Document Version
Final published version

Licence
CC BY

Geometry-Aware Edge-State Tracking for Robust Affine Formation Control

ZHONGGANG LI (Graduate Student Member, IEEE), **AND RAJ THILAK RAJAN** (Senior Member, IEEE)

Signal Processing Systems, EEMCS, Delft University of Technology, 2628CD Delft, The Netherlands

CORRESPONDING AUTHOR: ZHONGGANG LI (e-mail: z.li-22@tudelft.nl).

ABSTRACT Affine formation control (AFC) is a subset of formation control methods that enables co-ordinated multiagent movement while preserving affine relationships, and has recently gained increasing popularity due to its utility across diverse applications. AFC is inherently distributed, where each agent's local controller relies on the relative displacements of neighboring agents. The unavailability of these measurements in practice, due to node or communication failures, leads to a change in the underlying graph topology and subsequently causes instability or sub-optimal performance. In this work, each edge in the graph is modeled using a state-space framework, allowing the corresponding edge-states to be estimated with or without up-to-date measurements. We then propose a Kalman-based estimation framework where we fuse both temporal information from agents' dynamics and spatial information, which is derived from the geometry of the affine formations. We give convergence guarantees and optimality analysis on the proposed algorithm, and numerical validations show the enhanced robustness of AFC against these topology changes in several practical scenarios.

INDEX TERMS Formation control, Kalman filter, affine localization, decentralized control.

I. INTRODUCTION

Multiagent systems have been widely researched for their broad applications in various fields such as artificial intelligence [2], swarm robotics [3], social networks [4], and space applications [5], [6]. Distributed formation control is a fundamental task in a swarm where agents collectively preserve a geometric pattern, i.e., a formation, with application to collective object transport [7], space-based interferometry [8], or various sensing missions [9]. It relies on measurements of relative information among agents to achieve different formations. For instance, distance measurements are used to achieve rigid formations that allow translations and rotations [10], [11], bearing measurements allow formations with scaling of the geometry [12], [13], and displacements can be employed to realize affine formations [14].

Affine formation control (AFC) is a subset of displacement-based formation control, where the configurations of agents are allowed up to affine transformations over time, which include rotation, translation, shearing, or their combinations.

This flexibility is favored in complex and cluttered environments where the swarm must avoid certain obstacles. The agents can maintain a static formation [14] or track a time-varying target configuration with continuously changing affine transformations [15]. This maneuverability of affine formations is typically achieved by setting a small subset of agents as leaders, which can access global and absolute information. However, rigidity conditions are imposed on the underlying graph to ensure stability, which requires careful topology design. AFC is also a case of a networked control system [16], where information needs to be communicated over a network in which the communication pattern is defined by edges in a graph. Disruptions in sensing or communication, or an agent's malfunctioning in practice, will effectively change the underlying graph, which may cause stability and optimality issues. For a resilient deployment in harsh environments, strategies for topology changes are necessary.

Solutions to topology changes in networked control systems are abundant in the literature, from physical layers to

controller designs. The predominant strategy is to model a switched system with time-varying graphs [17], [18], [19], where the stability is shown for every allowed switch pattern. These works are suitable for various scenarios, including time-varying edge sets [17], [18] where there are no missing agents, and the time-varying vertex sets [19] where the uncontrolled or uncooperative nodes are considered in the switching pattern. However, AFC has a stringent graph rigidity condition to guarantee stability [14], which can be compromised by any missing edge or node in the predefined graph. This makes it difficult to design stabilizing patterns, especially for large-scale networks. Random and rapid changes in the graph pose additional challenges in the switched system.

Another line of work uses local predictors to estimate missing information originating from topology changes, such as packet dropouts [20], [21]. The philosophy is to design only one controller for a predefined graph and develop an additional observer or predictor for the control feedback. Examples of predictor design include Kalman filtering based on dynamic models [22], neural network-based prediction [23], etc. However, these solutions are not sensitive to the graph stability conditions and instead often rely on the availability of measurements to prevent error accumulation. For instance, permanent information loss, such as a departing or uncooperative node, is not tolerated. In the context of AFC, to the best of our knowledge, there is limited research to address the topological changes due to the above challenges.

In this paper, we develop a distributed estimation framework for topology changes due to missing information for the affine formation maneuver control of multiagent systems. We adopt a similar philosophy to [24] where each edge in the graph, representing the displacements used for local controllers, is modeled by a state-space tracking system. Due to the linearity of the model, a Kalman-based approach naturally suits this application, which offers computational advantages as compared to less interpretable and complex neural-based methods. In contrast to the conventional distributed Kalman filter, which breaks down in the presence of permanent measurement loss, we employ estimators that exploit the geometry information implicit in affine formations. We thus enable a unifying approach for several adverse scenarios challenging conventional methods in the context of AFC. This work expands on our preliminary results [1], where the general estimation framework is proposed with numerical verifications, but without detailed discussions on the guarantees and the performance of the algorithm. In this context, our additional contributions in this work include: 1) we enhance the feasibility in low observability conditions using a dynamic consensus filter; 2) we mathematically show the convergence properties for the adaptive convergence indicator, which indicate the quality of the geometric estimates; 3) the convergence and optimality of the proposed algorithm is shown; 4) additional simulations are added to verify the claimed properties, and to test the limits of our algorithms in larger networks.

Layout: Section II provides the preliminaries of the affine formation control, followed by the proposed adaptive edge

tracking modeling in Section III. In Section IV, we introduce the geometric estimators, which are then adaptively combined with direct edge measurements and dynamic predictions in our proposed geometry-aware relative Kalman filtering (GA-RKF) framework. The convergence and optimality of GA-RKF are discussed in Section V, and numerical validations of the proposed concepts and practical scenarios in Section VI. Finally, we conclude our work and give directions for future work in Section VII.

Notations: Vectors and matrices are represented by lowercase and uppercase boldface letters, respectively, such as $\mathbf{a}$ and $\mathbf{A}$. The elements of matrix $\mathbf{A}$ are expressed using $[\mathbf{A}]_{ij}$ where i and j denote the index of rows and columns, respectively. Sets and graphs are represented using calligraphic letters, e.g., $\mathcal{A}$. The relative complement of two sets is denoted by \. Vectors of length N of all ones and zeros are denoted by $\mathbf{1}_N$ and $\mathbf{0}_N$, respectively. An identity matrix of size N is denoted by $\mathbf{I}_N$. The Kronecker product is $\otimes$ and a vectorization of a matrix is denoted by $\text{vec}(\cdot)$ by stacking all the columns vertically. The trace operator is denoted by $\text{tr}(\cdot)$. We also use subscripts k on vectors and matrices to indicate a time-varying variable.

II. PRELIMINARIES
A. GRAPH THEORY

We consider N mobile agents in a D-dimensional space with D typically being 2 or 3. The prescribed interactions among the agents are described by an undirected *nominal graph* $\mathcal{G} = (\mathcal{V}, \mathcal{E})$ where the set of vertices is $\mathcal{V} = \{1, \ldots, N\}$ and the set of edges is $\mathcal{E} \subseteq \mathcal{V} \times \mathcal{V}$. As an undirected graph is equivalent to a bidirectional graph, i.e., $(i, j) \in \mathcal{E} \Leftrightarrow (j, i) \in \mathcal{E}$, we assume there are M directed edges (or $M/2$ undirected edges) in total. The set of neighbors of a node $i \in \mathcal{V}$ is defined as $\mathcal{N}_i = \{j \in \mathcal{V} : (i, j) \in \mathcal{E}\}$. In operation, the time-varying connectivity of the system is modeled by a *functional graph* $\mathcal{G}_k = (\mathcal{V}_k, \mathcal{E}_k)$ where k is the discrete-time index. The functional graph is a subgraph of the nominal graph for all time instances, i.e., $\mathcal{V}_k \subseteq \mathcal{V}$ and $\mathcal{E}_k \subseteq \mathcal{E}$ for all k. Correspondingly, the agents have a subset of neighbors $\mathcal{N}_{i,k} = \{j \in \mathcal{V} : (i, j) \in \mathcal{E}_k\}$, whose cardinality is denoted using a shorthand notation $N_{i,k} = |\mathcal{N}_{i,k}|$. The difference between functional and nominal graphs represents the failure of nodes and edges.

In this work, a frequently used graph characterization is the incidence matrix, and its definition for the functional graph $\boldsymbol{B}_k \in \mathbb{R}^{N \times M_k}$ where $M_k = \sum_{i \in \mathcal{V}_k} N_{i,k}$ is defined as

$$[\boldsymbol{B}_k]_{im} = \begin{cases} 1 & \text{if edge } e_m = (i, j) \in \mathcal{E}_k \text{ leaves node } i \\ -1 & \text{if edge } e_m = (i, j) \in \mathcal{E}_k \text{ enters node } i, \\ 0 & \text{otherwise} \end{cases}$$

(1)

which admits the structure $\boldsymbol{B}_k = [\boldsymbol{B}_{1,k}, \boldsymbol{B}_{2,k}, \ldots, \boldsymbol{B}_{N,k}]$ where the matrix $\boldsymbol{B}_{i,k} \in \mathbb{R}^{N \times N_{i,k}}, \forall i \in \mathcal{V}$, groups the columns per agent. Note that $\mathbf{1}_N^\top \boldsymbol{B}_{i,k} = \mathbf{0}_{N_{i,k}}^\top$. Fig. 1 shows an example of $\boldsymbol{B}_k$ for a functional graph derived from a 4-node complete nominal graph.

$$B_k = \begin{bmatrix} 1 & 1 & 1 & -1 & 0 & -1 & 0 & 0 & 0 & 0 \\ -1 & 0 & 0 & 1 & 1 & 0 & -1 & 0 & -1 & 0 \\ 0 & -1 & 0 & 0 & -1 & 1 & 1 & 1 & 0 & -1 \\ 0 & 0 & -1 & 0 & 0 & 0 & 0 & -1 & 1 & 1 \end{bmatrix}$$
$$\underbrace{\qquad}_{B_{1,k}} \quad \underbrace{\qquad}_{B_{2,k}} \quad \underbrace{\qquad}_{B_{3,k}} \quad \underbrace{\qquad}_{B_{4,k}}$$

FIGURE 1. An example of the incidence matrix B_k, which implies 10 (directed) edges. Note that this graph has fewer edges compared to its fully connected nominal counterpart.
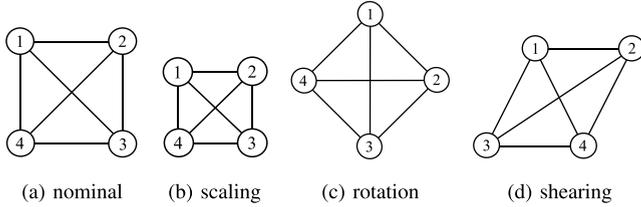

(a) nominal   (b) scaling   (c) rotation   (d) shearing

FIGURE 2. An illustration of a few basic affine transformations.

B. GEOMETRIC TRANSFORMATIONS

We define $z_{i,k} \in \mathbb{R}^D$ as the time-varying position of agent i at time instant k, and collect all the positions of the agents in a *configuration matrix* $Z_k = [z_{1,k}, z_{2,k}, \ldots, z_{N,k}] \in \mathbb{R}^{D \times N}$. Similarly, a *target configuration* that collects the expected positions of agents is defined as $Z_k^* = [z_{1,k}^*, z_{2,k}^*, \ldots, z_{N,k}^*] \in \mathbb{R}^{D \times N}$ in which $z_{i,k}^* \in \mathbb{R}^D$ is the individual target position for each agent $i \in \mathcal{V}$. For the nominal graph $\mathcal{G}$, we introduce a *nominal configuration* $P = [p_1, p_2, \ldots, p_N] \in \mathbb{R}^{D \times N}$ where $p_i \in \mathbb{R}^D$ is the nominal position for agent i. The nominal configuration represents a general geometric pattern that the agents are expected to achieve, and the time-varying target configuration is a time-varying mapping from the nominal configuration through geometric transformations.

In the context of the affine formation control (AFC), the transformation is limited to affine transformations, which pose the following constraint

$$Z_k^* = \Theta_k^* P + t_k^* \mathbf{1}_N^\top, \tag{2}$$

where $\Theta_k^* \in \mathbb{R}^{D \times D}$ characterizes a shape transformation such as scaling, rotation, shearing, etc., and $t_k^* \in \mathbb{R}^D$ indicates a collective translation. Some illustrations of the affine shape transformation are shown in Fig. 2, and note that they pose constraints on the structure of the Θ_k^* matrix with a reduced degree of freedom. In summary, the continuous target positions, which form several trajectories, are generated by designing Θ_k^* and t_k^*, given the nominal positions of the agents. The goal for the formation maneuver control is to steer the agents such that their positions Z_k converge to and track the target Z_k^* with minimum error.

C. LEADER-FOLLOWER MANEUVER CONTROL

AFC is a consensus-based control that aims to steer the agents into their desired positions using relative information, i.e., displacements. Typically, a small subset of agents is set as

TABLE 1. Discrete-time control laws for AFC [15], [25].

Leaders	Control law
static	$u_{i,k} = -\sum\limits_{j \in \mathcal{N}_i} l_{ij} z_{ij,k}$
constant velocity	$u_{i,k} = -\alpha \sum\limits_{j \in \mathcal{N}_i} l_{ij} z_{ij,k} - \eta \sum\limits_{\tau=0}^{k} \sum\limits_{j \in \mathcal{N}_i} l_{ij} z_{ij,\tau}$
varying velocity	$u_{i,k} = -\dfrac{1}{\gamma_i} \sum\limits_{j \in \mathcal{N}_i} l_{ij}(z_{ij,k} - \dot{z}_{j,k})$

leaders that globally track the target positions while still interacting with the remaining majority, i.e., the set of *followers*. In this scheme, target configurations Z_k^* are achieved but not informed to the followers if they maintain the formation. In other words, the geometry patterns for the maneuvers are described by the leaders. To achieve AFC, the number of leaders required is $D + 1$ with some geometrical conditions and typically $N \gg D + 1$ [15]. Hence, we limit our discussions to the followers in terms of control laws, edge and node failures, and the prospective estimator designs in this work.

In this work, we model the agents' motion using single-integrator dynamics in discrete time, which is a common and effective kinematic model for multiagent systems wherein the agent's velocity can be directly controlled. The dynamics for each agent $i \in \mathcal{V}_f$ are then given by

$$z_{i,k+1} = z_{i,k} + \Delta t u_{i,k}, \tag{3}$$

where Δt is a small time interval and $u_{i,k}$ is the velocity input. The control laws for various scenarios are shown in Table 1 [15], [25]. Here, we use a shorthand notation for the displacements i.e., $z_{ij,k} = z_{i,k} - z_{j,k}$ and the edge weights $l_{ij}, \forall (i, j) \in \mathcal{E}$ are associated with a nominal graph. The rigidity of the nominal graph guarantees the existence of stabilizing weights [14], which can be calculated through convex programs [14], [26] or mixed-integer programs [27] given the graph design. We initially assume the nominal graph satisfies the rigidity constraints, ensuring the stability of the control laws in Table 1, and later focus on realistic scenarios where such rigidity conditions may not hold.

Definition 1. (Sufficient formation convergence): We claim that the agents have sufficiently converged to their target positions at a given time instance k if

$$\delta_k = \frac{1}{N} \|Z_k - Z_k^*\|_{\mathrm{F}}^2 \leq \varepsilon, \tag{4}$$

with an arbitrarily small ε.

In AFC frameworks [15], [27], [28], [29], the tracking error δ_k is a common performance metric, which globally indicates the convergence of the algorithm. Sufficient convergence is asymptotically satisfied for controllers in Table 1 with no or bounded measurement noise, but can be violated at formation initialization or under large environmental disturbances before re-stabilization.
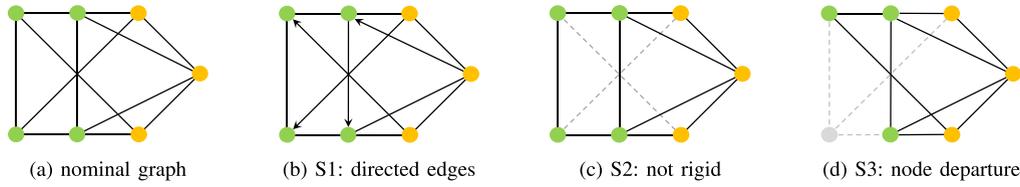
FIGURE 3. Some practical scenarios modeled by functional graphs, which are subgraphs of a nominal graph. The colored nodes and solid edges represent true agents and connections; orange nodes are candidates for leaders; gray nodes and dashed edges are unavailable agents and connections in the functional graph. The edges with arrows are directed edges representing one-way flow of information.

III. PROBLEM FORMULATION

A. MOTIVATION FOR EDGE-STATE ESTIMATION

In the previous section, we introduced formation controllers associated with a time-invariant nominal graph with certain rigidity conditions. In reality, these conditions are often not satisfied due to various practical challenges, e.g., imperfect communication channels that lead to one-way communication links, or limited sensing range that results in the loss of edges that violate the stabilizing rigidity conditions. This can also be due to hardware failures that require agents to leave the formation temporarily. These scenarios are illustrated in Fig. 3 and described below.

(S1) *One-way communication links:* During operation, there could be instances when information flows only in one direction, resulting in a directed functional graph, as shown in Fig. 3(b). Several existing controllers have been designed for directed topologies [28], but these solutions are generally incapable of randomly and potentially rapidly changing topologies.

(S2) *Violation of stabilizing conditions:* A realization of the functional graph might not satisfy the required rigidity conditions for the existence of stabilizing controllers. See an example scenario in Fig. 3(c), in which the graph can lose rigidity after removing one or more edges.

(S3) *Departing and rejoining agents:* In practice, it is common for agents to depart from the swarm due to failure or battery life, as shown in Fig. 3(d). In this case, the rest of the agents are still expected to maintain the formation in the absence of missing agents. In such situations, the controllers designed for the original topology are no longer effective.

To overcome these adverse scenarios, we design a state-space model for each edge, whose availability over time is modeled as intermittent observations. Furthermore, we explore the geometry of the formation that contains additional edge information to improve the estimator. Given this model, we could apply filtering and prediction techniques without having to redesign controllers or introduce switching systems.

B. RELATIVE STATE SPACE MODEL

In this section, we introduce the edge-state tracking model and later develop estimators based on this model. For each edge $(i,j) \in \mathcal{E}$ in the nominal graph, we assign a state vector $\boldsymbol{\gamma}_{ij,k} = [\boldsymbol{z}_{ij,k}^\top, \dot{\boldsymbol{z}}_{ij,k}^\top, \ddot{\boldsymbol{z}}_{ij,k}^\top]^\top \in \mathbb{R}^{3D}$ which includes the

displacement $\boldsymbol{z}_{ij,k}$ and the corresponding higher-order kinematics such as (relative) velocities and accelerations. We then propose a linear state-space model as follows

$$\boldsymbol{\gamma}_{ij,k+1} = \boldsymbol{F}\boldsymbol{\gamma}_{ij,k} + \boldsymbol{w}_{ij,k}, \tag{5a}$$

$$\tilde{\boldsymbol{y}}_{ij,k} = \boldsymbol{G}\boldsymbol{\gamma}_{ij,k} + \tilde{\boldsymbol{v}}_{ij,k}, \tag{5b}$$

where $\boldsymbol{F} \in \mathbb{R}^{3D \times 3D}$ is the state transition matrix in the dynamical model, and $\boldsymbol{G} = [1 \quad 0 \quad 0] \otimes \boldsymbol{I}_D \in \mathbb{R}^{D \times 3D}$ is an observation matrix that selects only the observation of the displacement i.e., $\tilde{\boldsymbol{y}}_{ij,k} \in \mathbb{R}^D$. The noises $\boldsymbol{w}_{ij,k} \sim \mathcal{N}(\boldsymbol{0}, \boldsymbol{Q}_{ij})$ and $\tilde{\boldsymbol{v}}_{ij,k} \sim \mathcal{N}(\boldsymbol{0}, \tilde{\boldsymbol{R}}_{ij,k})$ are assumed to be zero-mean Gaussian. Since this state-space model is based on relative kinematics (upto a translation), we also refer to (5) as the relative state-space model.

The edge estimation model operates as an independent observer within the architecture, and thus decouples it from the specific control dynamics (e.g., single-integrator). This independence allows users to select a more descriptive relative state-space model for enhanced performance. We therefore adopt a constant acceleration model among several common choices [30], without loss of generality. The matrices in this model are in standard form

$$\boldsymbol{F} = \begin{bmatrix} 1 & \Delta t & \frac{1}{2}\Delta t^2 \\ 0 & 1 & \Delta t \\ 0 & 0 & 1 \end{bmatrix} \otimes \boldsymbol{I}_D, \tag{6}$$

$$\boldsymbol{Q}_{ij} = \sigma_w^2 \begin{bmatrix} \frac{\Delta t^4}{4} & \frac{\Delta t^3}{2} & \frac{\Delta t^2}{2} \\ \frac{\Delta t^3}{2} & \Delta t^2 & \Delta t \\ \frac{\Delta t^2}{2} & \Delta t & 1 \end{bmatrix} \otimes \boldsymbol{I}_D, \tag{7}$$

where the variance σ_w^2 can be tuned.

For the observation model (5b), the state vector measurements should be incorporated, if available. However, these measurements may be unavailable due to various practical challenges discussed in the earlier section. In this case, we propose geometric estimators exploiting the affine formation properties of the network. Therefore, the observation model should choose either the available measurements or the geometric solution. The composite observation $\tilde{\boldsymbol{y}}_{ij,k}$ is then

$$\tilde{\boldsymbol{y}}_{ij,k} = \begin{cases} \boldsymbol{y}_{ij,k}, & \text{if } (i,j) \in \mathcal{E}_k \\ \hat{\boldsymbol{z}}_{ij,k}^{\text{geo}}, & \text{if } (i,j) \in \mathcal{E} \setminus \mathcal{E}_k \end{cases}, \tag{8}$$
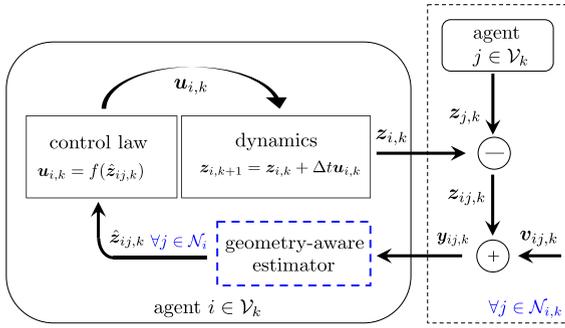
FIGURE 4. A general architecture of the formation control with our proposed geometry-aware estimator.

where

$$y_{ij,k} = z_{ij,k} + v_{ij,k}, \quad (9)$$

is the observation available to agent i with noise $v_{ij,k} \sim \mathcal{N}(\mathbf{0}, \mathbf{R}_{ij})$ under nominal conditions. The vector $\hat{z}_{ij,k}^{\text{geo}}$ denotes the geometric estimation of the edge state for $(i,j) \in \mathcal{E} \setminus \mathcal{E}_k$, i.e., when the measurement is missing at time instance k. The covariance $\tilde{\mathbf{R}}_{ij,k}$ for the equivalent noise $\tilde{v}_{ij,k}$ corresponds to the observation model (8)

$$\tilde{\mathbf{R}}_{ij,k} = \begin{cases} \mathbf{R}_{ij}, & \text{if } (i,j) \in \mathcal{E}_k \\ \mathbf{R}_{ij,k}^{\text{geo}} + \psi_{i,k}\mathbf{I}_D, & \text{if } (i,j) \in \mathcal{E} \setminus \mathcal{E}_k \end{cases}, \quad (10)$$

where $\mathbf{R}_{ij}$ is the noise covariance related to the direct measurement (9), and $\mathbf{R}_{ij,k}^{\text{geo}}$ is the covariance for the geometric estimator, which is then adaptively penalized by $\psi_{i,k}\mathbf{I}_D$ based on the confidence of the geometric estimation. Here, the adaptive coefficient $\psi_{i,k}$ approximates the state of convergence, which introduces a large penalty when the nodes are in random configuration, e.g., during initialization, and is negligible when the target configuration is reached.

Given the relative state-space model (5), we aim to propose adaptive filters to estimate the edge state from noisy and incomplete measurements. The estimated state could be subsequently used by the local controllers for position updates. In the following section, we present the details of the geometric estimators and discuss their performances. A general system architecture is shown in Fig. 4, where the differences compared with an ideal system are highlighted, i.e., estimators are deployed for unobservable neighbors.

IV. GEOMETRY-AWARE ESTIMATORS
In this section, we propose a geometric estimator and discuss the theoretical limitations and extensions. We later fuse it into a Kalman filter framework as our proposed geometric solution for $\hat{z}_{ij,k}^{\text{geo}}$ introduced in (8).

A. RELATIVE AFFINE LOCALIZATION
Observe that the configuration space is determined by a lower-dimensional parameter space defined by the geometric parameters $\mathbf{\Theta}_k^*$ and t_k^*, as evident from equation (2). As

such, missing configurations can be estimated by first reconstructing this parameter space. This is a geometrical way of localizing (relative) positions, which we refer to as Relative Affine Localization (RAL). This technique assumes sufficient formation convergence as in Definition 1 such that $z_{i,k}$ is sufficiently close to $z_{i,k}^*$ for $i \in \mathcal{V}$.

The local form of the geometry constraint (2) is $z_{i,k}^* = \mathbf{\Theta}_k^* p_i + t_k^*$, $\forall i \in \mathcal{V}$ and observe that

$$z_{ij,k}^* = z_{i,k}^* - z_{j,k}^* = \mathbf{\Theta}_k^* p_i + t_k^* - (\mathbf{\Theta}_k^* p_j + t_k^*) = \mathbf{\Theta}_k^* p_{ij}, \quad (11)$$

for $i \in \mathcal{V}, j \in \mathcal{N}_i$, where $p_{ij} \triangleq p_i - p_j$ comes from the known nominal configuration. Thus $z_{ij,k}$ is linear w.r.t. $\mathbf{\Theta}_k^*$, and the observations (9) can be extend to $y_{ij,k} = z_{ij,k} + v_{ij,k} = \mathbf{\Theta}_k^* p_{ij} + v_{ij,k}$ under the assumption of sufficient formation convergence. If for each node $i \in \mathcal{V}_k$, we collect all the observations $y_{ij,k}, \forall j \in \mathcal{N}_{i,k}$ column-wise in a matrix $\mathbf{Y}_{i,k} \in \mathbb{R}^{D \times N_{i,k}}$, we have a local aggregated set of equations

$$\mathbf{Y}_{i,k} = \mathbf{\Theta}_k^* \mathbf{H}_{i,k} + \mathbf{V}_{i,k}, \quad (12)$$

where $\mathbf{H}_{i,k} = \mathbf{P}\mathbf{B}_{i,k} \in \mathbb{R}^{D \times N_{i,k}}$, $\mathbf{B}_{i,k}$ is the incidence block of agent i from the functional graph defined in (1), and $\mathbf{V}_{i,k} \in \mathbb{R}^{D \times N_{i,k}}$ collects the corresponding noise $v_{ij,k}$ in columns. The geometry parameters $\mathbf{\Theta}_k^*$ can then be estimated through a least-square formulation

$$\hat{\mathbf{\Theta}}_{i,k}^{\text{ral}} = \arg\min_{\mathbf{\Theta}_k^*} \|\mathbf{\Theta}_k^* \mathbf{H}_{i,k} - \mathbf{Y}_{i,k}\|_{\text{F}}^2 = \mathbf{Y}_{i,k}\mathbf{H}_{i,k}^\dagger, \quad (13)$$

where $\mathbf{H}_{i,k}^\dagger = \mathbf{H}_{i,k}^\top(\mathbf{H}_{i,k}\mathbf{H}_{i,k}^\top)^{-1}$. The reconstruction of the unobservable edge $\hat{z}_{ij,k}^{\text{ral}}, \forall j \in \mathcal{N}_i \setminus \mathcal{N}_{i,k}$ can be subsequently obtained by

$$\hat{z}_{ij,k}^{\text{ral}} = \hat{\mathbf{\Theta}}_{i,k}^{\text{ral}} p_{ij} = \mathbf{Y}_{i,k}\mathbf{H}_{i,k}^\dagger p_{ij}, \quad (14)$$

with a covariance structure

$$\mathbf{R}_{ij,k}^{\text{ral}} = \left(p_{ij}^\top \mathbf{H}_{i,k}^{\dagger\top} \otimes \mathbf{I}_D\right)\left(\mathbf{I}_{N_{i,k}} \otimes \mathbf{R}_{ij}\right)\left(p_{ij}^\top \mathbf{H}_{i,k}^{\dagger\top} \otimes \mathbf{I}_D\right)^\top. \quad (15)$$

This is the RAL solution and the derivation of (15) is shown in Appendix A, and a unique solution using (14) is guaranteed if $\mathbf{H}_{i,k}$ is of full row rank, which translates to some geometric conditions which we refer to as *geometric feasibility*, and define as follows.

Definition 2. (Geometric feasibility of RAL): Relative affine localization is geometrically feasible if the estimator (14) has a unique solution for agent i, when $N_{i,k} \geq D$, i.e., $\mathbf{Y}_{i,k}$ contains observations of at least D neighboring agents that are not collinear in $\mathbb{R}^2$ or coplanar in $\mathbb{R}^3$ in the nominal configuration, to ensure a full-rank $\mathbf{H}_{i,k}$. A few examples in $\mathbb{R}^2$ are illustrated in Fig. 5 .

Although RAL applies in most cases, we are still interested in providing viable solutions in more extreme cases, i.e., for some time instance k, geometric feasibility is not satisfied. Since the leaders in the formation determine the maneuvering pattern, the formation can present special cases of affine transformation, such as scaling and rotation, etc., in a controlled
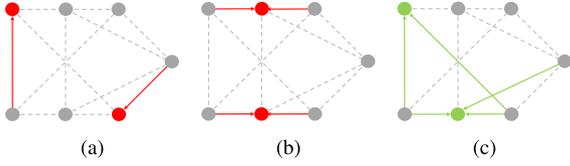
FIGURE 5. A few examples to explain geometric feasibility of RAL in $\mathbb{R}^2$, where the colored nodes represent the agents of interest. (a) infeasible due to $N_{i,k} < D$ locally. (b) infeasible due to collinear neighbors such that $H_{i,k}$ is not full-rank. (c) feasible.

manner. In these cases, $\boldsymbol{\Theta}_k^*$ is structured, which we can use as constraints for estimation (14) for a further reduction of the required number of observations. We give a broad overview of this approach in Appendix B. Another more general solution, which we provide in the following, is to allow agents to share their estimates of the geometry parameters using a consensus filter.

B. CONSENSUS FILTERING

In scenarios where geometric feasibility is not met, agents can estimate $\boldsymbol{\Theta}_k^*$ using a consensus that exploits neighborhood communication. Due to the time-varying nature of the parameter of interest, i.e., $\boldsymbol{\Theta}_k^*$, we propose the use of the following dynamic consensus filter [31], which has the following updates

$$\Delta\hat{\boldsymbol{\Theta}}_{i,k} = \sum_{j \in \mathcal{N}_{i,k}} \left(\hat{\boldsymbol{\Theta}}_{j,k} - \hat{\boldsymbol{\Theta}}_{i,k} \right) + \sum_{j \in \mathcal{I}_{i,k}} \left(\hat{\boldsymbol{\Theta}}_{j,k}^{\mathrm{ral}} - \hat{\boldsymbol{\Theta}}_{i,k} \right),$$
(16a)

$$\hat{\boldsymbol{\Theta}}_{i,k+1} = \hat{\boldsymbol{\Theta}}_{i,k} + \epsilon \Delta\hat{\boldsymbol{\Theta}}_{i,k},$$
(16b)

where $\hat{\boldsymbol{\Theta}}_{i,k}$ are the parameters of interest for agent i, RAL estimates $\hat{\boldsymbol{\Theta}}_{j,k}^{\mathrm{ral}}$ from (13) can be considered as external inputs that contains the information of the underlying time-varying signal, and ϵ is a small constant multiplied by the increment $\Delta\hat{\boldsymbol{\Theta}}_{i,k}$. The set $\mathcal{I}_{i,k}$ contains both the neighbors and the agent i, i.e., $\mathcal{I}_{i,k} = \mathcal{N}_{i,k} \cup \{i\}$. The time-varying set of neighbors $\mathcal{N}_{i,k}$ implies an intermittent communication pattern, and the convergence analysis of such behavior can be found in e.g., [32].

Given this filtered estimate $\hat{\boldsymbol{\Theta}}_{i,k}$, the final geometric estimation is $\hat{\boldsymbol{z}}_{ij,k}^{\mathrm{geo}} = \hat{\boldsymbol{\Theta}}_{i,k} \boldsymbol{p}_{ij}$, which has a reduced covariance compared with using $\hat{\boldsymbol{\Theta}}_{i,k}^{\mathrm{ral}}$ without the consensus filter. The covariance of this estimate is also reduced by approximately a factor of N from (15)

$$\boldsymbol{R}_{ij,k}^{\mathrm{geo}} = \boldsymbol{R}_{ij,k}^{\mathrm{ral}} / N.$$
(17)

A more detailed derivation can be found in Appendix A.

C. LOCAL CONVERGENCE INDICATOR

Recall from Section IV that the RAL estimator assumes sufficient formation convergence. When this is not satisfied, $\hat{\boldsymbol{z}}_{ij,k}^{\mathrm{geo}}$ in observation model (8) is subject to large biases that can be destructive to the algorithm. This is the reason we introduce

the adaptive covariance matrix $\boldsymbol{R}_{ij,k}^{\mathrm{geo}} + \psi_{i,k}\boldsymbol{I}$ in (10) with a positive local convergence indicator (CI) $\psi_{i,k}$. An ideal indicator function would be the tracking error (4), which directly compares the difference between the agents' real and target positions. However, this is a global function that is locally intractable since the target configuration $\boldsymbol{Z}_k^*$ is not known to the follower agents. Therefore, we propose the following CI

$$\psi_{i,k} = \frac{1}{N_{i,k}} \sum_{j \in \mathcal{N}_{i,k}} \left\| \hat{\boldsymbol{\Theta}}_{i,k}^{\mathrm{ral}} - \hat{\boldsymbol{\Theta}}_{j,k}^{\mathrm{ral}} \right\|_{\mathrm{F}}^2,$$
(18)

where $\hat{\boldsymbol{\Theta}}_{i,k}^{\mathrm{ral}}$ is the local estimate of the geometry parameters, and $\hat{\boldsymbol{\Theta}}_{j,k}^{\mathrm{ral}}$ is accessible through neighborhood communication. In contrast to (4), our proposed CI (18) requires no global information but exhibits a similar trend as the tracking error δ_k, which is suitable as the adaptive penalty of the covariance. An intuitive graphical explanation of this CI is shown in Fig. 6, and we give some formal mathematical guarantees in the following sections.

D. GEOMETRY-AWARE RELATIVE KALMAN FILTER

We now reexamine the edge state-space model (5) and propose our edge-state tracking algorithm. Disregarding the geometric estimator $\hat{\boldsymbol{z}}_{ij,k}^{\mathrm{geo}}$ in (8), a Kalman filter with intermittent observations can be derived from the tracking model (5), where the predictions based on the dynamical model are run for all time steps but the correction steps are executed only when direct edge observations $\boldsymbol{y}_{ij,k}$ are available. We name this modified Kalman filter as *Relative Kalman Filter* (RKF) ([1] Section III-B), as we focus on the edges that denote the relative state space. If the geometric estimator $\hat{\boldsymbol{z}}_{ij,k}^{\mathrm{geo}}$ in (8) is provided, we use it as an alternative source of observations to extend the RKF framework with extra correction steps, which is coined *Geometry-Aware Relative Kalman Filter* (GA-RKF), which is outlined in Algorithm 1.

V. CONVERGENCE AND OPTIMALITY

In this section, we give insights into the conditions of convergence and optimality of the proposed GA-RKF algorithm. We also discuss the applicability and guarantees in practical scenarios. As is known, the convergence of a Kalman filter depends on the properties of the dynamic and observation matrices in the state-space model and the noise covariance. In our edge tracking case, the baseline framework is a constant acceleration model with intermittent observations (the RKF), which is well understood in the literature. We start our analysis with the adaptive coefficient $\psi_{i,k}$ in (10), i.e., convergence indicator (18).

A. CONVERGENCE INDICATOR

Recollect that our primary objective in introducing the convergence indicator (CI) $\psi_{i,k}$ in (18) is to penalize the covariance if sufficient formation convergence in Definition 1 is not satisfied. We show that $\psi_{i,k}$ qualifies as it converges the same way as the tracking error δ_k (4).
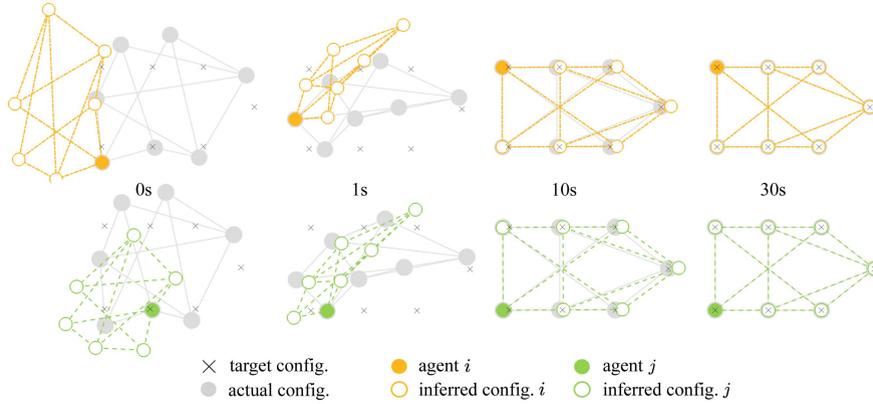
× target config.   ● agent i ● agent j
● actual config.   ○ inferred config. i ○ inferred config. j

FIGURE 6. An illustration of the convergence indicator at discrete time intervals of $0, 1, 10$ and 30 seconds. While the system has not sufficiently converged, e.g., at 1s, large discrepancies between $\hat{\Theta}_{i,k}^{\text{ral}}$ and $\hat{\Theta}_{j,k}^{\text{ral}}$ lead to different locally perceived formations, i.e., the inferred configurations $\hat{\Theta}_{i,k}^{\text{ral}} P$ and $\hat{\Theta}_{j,k}^{\text{ral}} P$. As the system converges to the target configuration, these discrepancies decrease until the agents reach a consensus on the perceived formation e.g., at 30s in this illustration. This implies that the global convergence can be approximated by gauging the difference between local and neighborhood estimations of $\hat{\Theta}_{i,k}^{\text{ral}}$, i.e., CI (18).

Algorithm 1: *GA-RKF*, for Agent $i \in \mathcal{V}_k$ at Time Instant k.

1: **Input**: Dimensions D, Number of neighbors $N_{i,k}$ and Measurements $\boldsymbol{Y}_{i,k} \in \mathbb{R}^{D \times N_{i,k}}$ (12)
2: **Output**: Estimates $\hat{\boldsymbol{z}}_{ij,k}$ for edge $(i,j) \in \mathcal{E}$
3: Construct $\boldsymbol{H}_{i,k}$ corresponding to $\boldsymbol{Y}_{i,k}$
4: **if** $N_{i,k} \geq D$ and $\boldsymbol{H}_{i,k}$ is full rank **then**
5:   Compute $\hat{\boldsymbol{\Theta}}_{i,k}^{\text{ral}}$ from (13)
6: **else**
7:   Set $\hat{\boldsymbol{\Theta}}_{i,k}^{\text{ral}} = \boldsymbol{0}$
8: **end if**
9: Exchange $\hat{\boldsymbol{\Theta}}_{i,k-1}$ and $\hat{\boldsymbol{\Theta}}_{i,k}^{\text{ral}}$ with neighbors $j \in \mathcal{N}_{i,k}$
10: Compute convergence indicator $\psi_{i,k}$ from (18)
11: Compute $\hat{\boldsymbol{\Theta}}_{i,k}$ from (16)   ▷ Consensus filtering
12: **for** $j \in \mathcal{N}_i$ **do**   ▷ Edge-state tracking
13:   **if** $(i,j) \notin \mathcal{E}_k$ **then**
14:     Compute $\hat{\boldsymbol{z}}_{ij,k}^{\text{geo}} = \hat{\boldsymbol{\Theta}}_{i,k} \boldsymbol{p}_{ij}$
15:     Compute $\boldsymbol{R}_{ij,k}^{\text{geo}} + \psi_{i,k} \boldsymbol{I}_D$ from (15) and (17)
16:   **end if**
17:   $\boldsymbol{K}_{ij,k} = \boldsymbol{\Lambda}_{ij,k-1} \boldsymbol{G}^\top (\tilde{\boldsymbol{R}}_{ij,k} + \boldsymbol{G} \boldsymbol{\Lambda}_{ij,k-1} \boldsymbol{G}^\top)^{-1}$
18:   $\hat{\boldsymbol{\gamma}}_{ij,k} = \hat{\boldsymbol{\gamma}}_{ij,k-1} + \boldsymbol{K}_{ij,k}(\tilde{\boldsymbol{y}}_{ij,k} - \boldsymbol{G} \hat{\boldsymbol{\gamma}}_{ij,k-1})$
19:   $\boldsymbol{\Lambda}_{ij,k} = (\boldsymbol{I} - \boldsymbol{K}_{ij,k} \boldsymbol{G}) \boldsymbol{\Lambda}_{ij,k-1}$ ▷ Kalman iterations
20:   $\hat{\boldsymbol{z}}_{ij,k} = \boldsymbol{G} \hat{\boldsymbol{\gamma}}_{ij,k}$
21: **end for**

Lemma 1: (Upper bound of CI): In the noiseless case, i.e., $\boldsymbol{v}_{ij,k} = 0 \ \forall (i,j) \in \mathcal{E}_k$, the local convergence indicator $\psi_{i,k}$ (18) is upper bounded by the tracking error δ_k (4) as $\psi_{i,k} \leq c_{i,k} \delta_k$, where $c_{i,k} \geq 0$ is a time-varying scalar given by

$$c_{i,k} = \frac{N}{N_{i,k}} \sum_{j \in \mathcal{N}_{i,k}} \left\| \boldsymbol{B}_{i,k} \boldsymbol{H}_{i,k}^\dagger - \boldsymbol{B}_{j,k} \boldsymbol{H}_{j,k}^\dagger \right\|_{\text{F}}^2, \quad (19)$$

with known $\boldsymbol{B}_{i,k}$ and $\boldsymbol{H}_{i,k}^\dagger$ from RAL solutions (14).

Proof: See Appendix C   ∎

Lemma 1 proves that if the tracking error δ_k follows a certain trend under standard control laws, i.e., asymptotically and exponentially converges to zero, then the local indicator $\psi_{i,k}$ will also converge similarly up to a known scaling. In the noisy case, it is intuitive that similar conclusions hold, which is formalized in the following theorem.

Theorem 1. (Upper bound of CI under observation noises): Under observation model (12), the expectation of the local convergence indicator $\mathbb{E}[\psi_{i,k}]$ is upper bounded by the expectation of the tracking error $\mathbb{E}[\delta_k]$ up to a known scaling and an offset, i.e, $\mathbb{E}[\psi_{i,k}] \leq c_{i,k} \mathbb{E}[\delta_k] + b_{i,k}$, where

$$c_{i,k} = \frac{N}{N_{i,k}} \sum_{j \in \mathcal{N}_{i,k}} \left\| \boldsymbol{B}_{i,k} \boldsymbol{H}_{i,k}^\dagger - \boldsymbol{B}_{j,k} \boldsymbol{H}_{j,k}^\dagger \right\|_{\text{F}}^2, \quad (20a)$$

$$b_{i,k} = \frac{tr(\boldsymbol{R}_{ij})}{N_{i,k}} \sum_{j \in \mathcal{N}_{i,k}} \left(\left\| \boldsymbol{H}_{i,k}^\dagger \right\|_{\text{F}}^2 + \left\| \boldsymbol{H}_{j,k}^\dagger \right\|_{\text{F}}^2 \right). \quad (20b)$$

Proof: See Appendix C.   ∎

In the presence of noise, a biased term related to the noise covariance appears in the inequality. In this case, we claim that if the noise energy is finite and the tracking error converges to zero with a small margin of error, CI also converges to a finite value.

Remark 1: (Sufficiency for CI convergence): The convergence of the tracking error (4) is a sufficient but not a necessary condition for the convergence of the CI (18), i.e., if $\delta_k \to 0$, then $\psi_{i,k} \to 0$ as $k \to \infty$.

The sufficiency of CI convergence is obvious given the upper bounds in Lemma 1 and Theorem 1, but the necessity is generally not true. Note that the definition of CI (18) only requires agreement of geometry parameters with the neighboring agents, i.e., only shape convergence of the formation is considered, but not the translations. For instance, if the formation converges to the target configuration up to a large

translation, indicators $\psi_{i,k}$ for all i will be zero, but the tracking error will be large. In practice, the setting of leaders will ensure convergence to the target configuration, and $\psi_{i,k}$ can be used to benchmark global convergence.

B. CONVERGENCE OF GA-RKF

In this section, we give insights into the convergence of Algorithm 1. We begin by analyzing the baseline version of the RKF algorithm, which is a standard Kalman filter with intermittent observations [33] without a geometric estimator. We model the availability of the edge observation as an i.i.d. Bernoulli process with parameter $0 \leq \lambda_{ij} \leq 1$. Here, $\lambda_{ij} = 1$ indicates that all observations are available at all time instances k for edge $(i, j) \in \mathcal{E}$, and $\lambda_{ij} = 0$ refers to the absence of any observations, i.e., the edge is permanently lost from the graph. We emphasize the case of $\lambda_{ij} = 0$, as this relates to the node failures scenario (see Section III-A).

If the geometric estimation is not considered, the edge state-space model (5) is simplified to

$$\gamma_{ij,k+1} = \boldsymbol{F}\gamma_{ij,k} + \boldsymbol{w}_{ij,k}, \tag{21a}$$

$$\boldsymbol{y}_{ij,k} = \boldsymbol{G}\gamma_{ij,k} + \boldsymbol{v}_{ij,k}, \tag{21b}$$

with $\boldsymbol{v}_{ij,k} \sim \mathcal{N}(\boldsymbol{0}, \boldsymbol{R}_{ij})$ and $\boldsymbol{w}_{ij,k} \sim \mathcal{N}(\boldsymbol{0}, \boldsymbol{Q}_{ij})$, and the observation availability is controlled by $\lambda_{ij} \; \forall (i, j) \in \mathcal{E}$. Matrices $\boldsymbol{F}$ and $\boldsymbol{G}$ are the same as given for model (5). Lemma 2 states the convergence of RKF from model (21).

Lemma 2. (Convergence of RKF): If $(\boldsymbol{F}, \boldsymbol{Q}_{ij}^{1/2})$ is controllable, $(\boldsymbol{F}, \boldsymbol{G})$ is detectable, and $\lambda_{ij} > 0$, then the estimation error covariance for RKF is bounded.

Proof: Let λ_c be a known critical threshold, then we know from [33] that if $\lambda_{ij} > \lambda_c$, then the Kalman filter with intermittent observations leads to a bounded error covariance. The proof of controllability and detectability of (21) is straightforward and thus omitted. The critical value λ_c in general is bounded by $\underline{\lambda} \leq \lambda_c \leq \bar{\lambda}$. However, the upper and lower bounds meet in our case of a constant acceleration model at $\lambda_c = 1 - 1/\alpha^2$ where α is the largest absolute eigenvalue of $\boldsymbol{F}$ (Sec IV, [33]). In this case, $\alpha = 1$ for the $\boldsymbol{F}$ matrix, which leads to $\lambda_{ij} > \lambda_c = 0$ as needed for the convergence. ∎

Remark 2: (Applicability of RKF): The claim in Lemma 2 is intuitive since the matrix $\boldsymbol{F}$ for the constant acceleration model represents a marginally stable system, which indicates that estimation covariance will be bounded without the supervision of many observations. For unstable systems in which $\alpha > 1$, the critical value λ_c will increase, indicating that frequent observations are needed for the covariance to be bounded. From an information-theoretic perspective, the Mahler measure [34] can also be used to determine the minimum data rates for stability, which yields the same threshold as our analysis. However, RKF diverges once the edge is completely lost, i.e., $\lambda_{ij} = 0$, when certain nodes are missing from the graph.

In GA-RKF, geometric estimations provide extra edge observations, promoting the practical edge availability, especially when $\lambda_{ij} = 0$. The key is to ensure a finite observation covariance $\boldsymbol{R}_{ij,k}^{\text{geo}} + \psi_{i,k}\boldsymbol{I}_D$ in model (10) for the geometric estimator to qualify as an effective observation. Next, we present a general claim of the convergence of GA-RKF with an informal proof.

Proposition 1 (Convergence of GA-RKF): At time instance k, GA-RKF on all edges $(i, j) \in \mathcal{E}$ admits a finite estimation covariance for $0 \leq \lambda_{ij} \leq 1$, if geometric feasibility in Definition 2 is satisfied for agent i and the tracking error δ_k is bounded.

Proof: If geometric feasibility is satisfied, then $\boldsymbol{H}_{i,k}^{\dagger}$ in (15) is finite. According to Theorem 1, CI $\psi_{i,k}$ is also bounded if the tracking error δ_k is bounded. As such, the adaptive covariance $\boldsymbol{R}_{ij,k}^{\text{geo}} + \psi_{i,k}\boldsymbol{I}_D$ is also bounded across time to qualify as extra observations. Subsequently, the equivalent edge availability $\bar{\lambda}_{ij}$ under GA-RKF is guaranteed to be greater than the critical value shown in Lemma 2, i.e., $\bar{\lambda}_{ij} > \lambda_c = 0$ for the GA-RKF to converge. ∎

Remark 3: (Applicability of GA-RKF): In the scenario that geometric feasibility in Definition 2 is not satisfied for some agents, GA-RKF can achieve convergence since we implement the consensus filtering (16) to ensure estimates from immediate neighbors are available. Hence, GA-RKF can address the $\lambda_{ij} = 0$ case as compared to the RKF.

We have given insights into the convergence property of the proposed GA-RKF algorithm, which is widely applicable owing to the geometric estimator. On the other hand, these extra observations can potentially contribute to an improved estimation performance compared to RKF, which we elaborate next by comparing the estimation bounds.

C. POSTERIOR CRAMÉR-RAO BOUNDS

For a linear Gaussian state-space model, the Kalman filter is optimal, i.e., the posterior covariance is minimized and reaches the posterior Cramér-Rao bound (PCRB) [35]. The tracking model (21) is one such case, and thus the RKF algorithm is optimal. In this section, we show that GA-RKF outperforms RKF by showing that the PCRB of the state estimate using GA-RKF is lower than that of the bound on the state estimates obtained from RKF, due to the additional geometric observations. The Fisher information matrix (FIM) for RKF under model (21) at time instance k is

$$\boldsymbol{J}_{ij,k+1}^{\text{rkf}} = \beta_{ij,k}\boldsymbol{G}^{\top}\boldsymbol{R}_{ij}^{-1}\boldsymbol{G} + \left(\boldsymbol{Q}_{ij} + \boldsymbol{F}\boldsymbol{J}_{ij,k}^{\text{rkf}\,-1}\boldsymbol{F}^{\top}\right)^{-1}, \tag{22}$$

where $\beta_{ij,k}$ is a binary scalar indicating the observation availability, i.e, $\beta_{ij,k} = 0$ when no observations are available at time k. Similarly, the FIM for GA-RKF for model (5) is

$$\boldsymbol{J}_{ij,k+1}^{\text{ga-rkf}} = \beta_{ij,k}\boldsymbol{G}^{\top}\boldsymbol{R}_{ij}^{-1}\boldsymbol{G} + (1 - \beta_{ij,k})\boldsymbol{G}^{\top}$$
$$\left(\boldsymbol{R}_{ij,k}^{\text{geo}} + \psi_{i,k}\boldsymbol{I}_D\right)^{-1}\boldsymbol{G} + \left(\boldsymbol{Q}_{ij} + \boldsymbol{F}\boldsymbol{J}_{ij,k}^{\text{rkf}\,-1}\boldsymbol{F}^{\top}\right)^{-1}, \tag{23}$$

where there is an additional term for the extra geometric observations. Note that FIM is additive, since our geometric
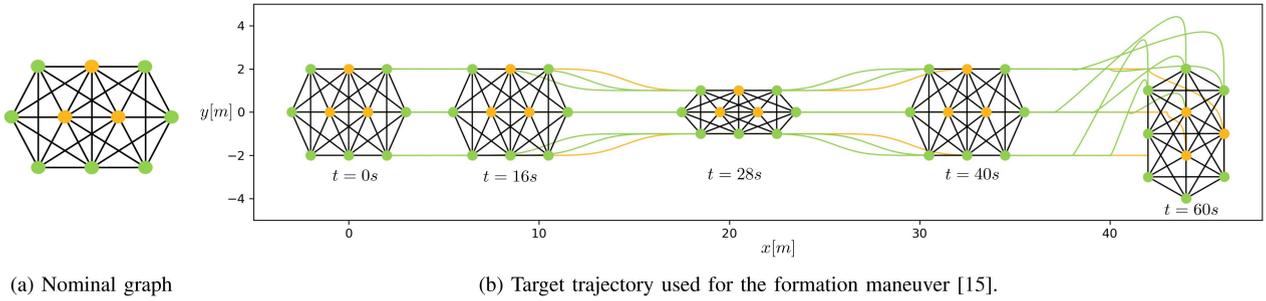
FIGURE 7. The nominal graphs and the target trajectories of the formation maneuver which are used for the simulation. The nodes in orange are selected as leaders, which will not be considered in the simulation scenarios.

estimates are independent of the direct observations. We now conclude the optimality in the following theorem.

Proposition 2 (Optimality of GA-RKF): The estimation covariance of GA-RKF reaches the PCRB (23), i.e., $\text{cov}(\hat{z}_{ij,k}) \succeq \boldsymbol{J}_{ij,k}^{\text{ga-rkf}\,-1}$ with equality, which is more optimal than PCRB for RKF (22), i.e., $\boldsymbol{J}_{ij,k}^{\text{rkf}\,-1} \succeq \boldsymbol{J}_{ij,k}^{\text{ga-rkf}\,-1}$.

Proof: It is straightforward to see that $\boldsymbol{J}_{ij,k}^{\text{ga-rkf}} \succeq \boldsymbol{J}_{ij,k}^{\text{rkf}}$ due to the extra positive definite term. The equality holds when $\beta_{ij,k} = 1$, i.e., all observations are direct observations and no geometric estimates are engaged. Then $\boldsymbol{J}_{ij,k}^{\text{rkf}\,-1} \succeq \boldsymbol{J}_{ij,k}^{\text{ga-rkf}\,-1}$ holds simply due to the Loewner ordering property [36]. ∎

To conclude the optimality of GA-RKF, the posterior covariance reaches the PCRB since it is still a linear Gaussian system, and its PCRB is lower than that of RKF, indicating its better optimality. The two PCRBs meet when all direct edge observations are available.

VI. SIMULATIONS

In this section, we present numerical validations of our proposed edge-state estimation algorithm and test it in several practical scenarios to show the enhanced robustness. We first introduce the simulation setup, where we give the nominal graphs, describe the maneuvering pattern, and various other system parameters. We then validate the optimality and convergence of the GA-RKF algorithm that is disconnected from the control loop. Finally, we show the performance of the GA-RKF algorithm when introduced into an affine formation control in some practical scenarios. The simulation code and plots are available online.[1]

A. SIMULATION SETUP

We consider a nominal graph in $\mathbb{R}^2$ for formation maneuvers [1], which is illustrated in Fig. 7(a), where there are $N = 10$ nodes with $M/2 = 30$ undirected edges. The maneuvering pattern used in the simulation is shown in Fig. 7(b), where we simulate for a duration of 60s with a discrete time step $\Delta t = 0.01$ s. Equivalently, the control and communication of the agents run at a frequency of 100Hz, which is feasible with modern embedded architectures. Recall from (2) that target
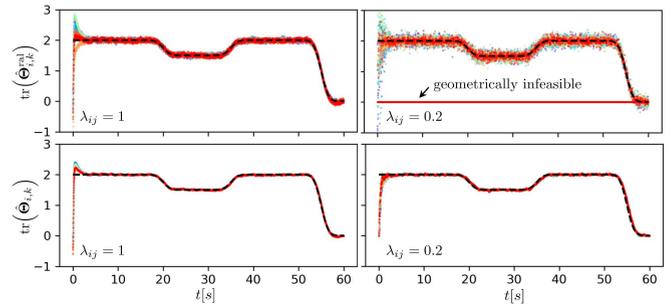
---
[1] https://github.com/asil-lab/zli-garkf-afc

FIGURE 8. Estimations of Θ_k^* with RAL (upper row) and consensus filtering (bottom row) over time under full and low observation settings. The black dashed line is the true values of $tr(\Theta_k^*)$ across time, and the colored dots are agents' local estimates. λ_{ij} characterize the Bernoulli distribution chosen the same for all edges $(i,j) \in \mathcal{E}$. If λ_{ij} is small (bottom), then a significant edge loss is present and geometric feasibility is violated more frequently, in which case $\hat{\Theta}_{i,k}^{ral}$ is set to zero.

trajectories $\boldsymbol{Z}_k^*$ at any time instance $k \leq 6000$ are determined by the underlying transformation parameters Θ_k^* and $\boldsymbol{t}_k^*$. The noise covariance $\mathbf{R}_{ij,k}$ for the observation model (9) is chosen as a constant $\sigma_v^2 \begin{bmatrix} 1 & 0.3 \\ 0.3 & 1 \end{bmatrix} \forall k$, where we select $\sigma_v = 0.1$ which is a nominal value used in various experiments. For the step size ϵ in the consensus filter (16), the estimation accuracy can be compromised when it is tuned too large, and can lag the parameter of interest if tuned too small. We choose a mild $\epsilon = 0.08$ for a decent performance.

B. GEOMETRY-AWARE ESTIMATORS

To validate the theoretical claims in Section V, we first show the following results independent from the formation control, i.e., the estimates $\hat{z}_{ij,k}$ from Algorithm 1 are not introduced in the controller, which instead uses complete information.

As discussed in Section IV-A, the estimation of Θ_k^* is conditioned on geometric feasibility, and the consensus filtering in Section IV-B is proposed to relax the condition by allowing the exchange of the estimates in the neighborhood. The estimation covariance (17) is reduced at the same time. Fig. 8 shows the tracking performance of the geometric estimators, where it is clearly shown that consistent estimates can be provided even when there are significant edge losses using the
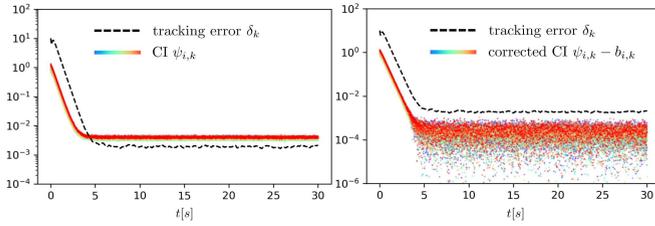
FIGURE 9. The relationship between the tracking error δ_k and the convergence indicator $\psi_{i,k}$. Only the first $30s$ is simulated and the mean of 100 Monte Carlo experiments is presented.

FIGURE 11. Tracking errors δ_k under random edge losses (left) with $\lambda_{ij} = 0.4$, and the tracking error $\bar{\delta}$ is averaged across time k (right).
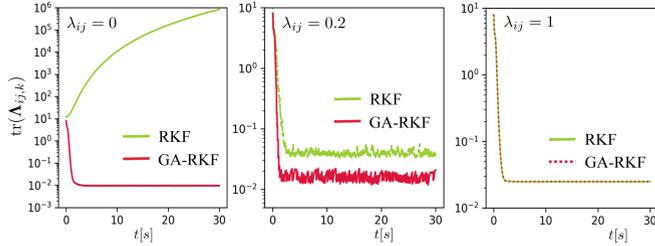

FIGURE 10. The convergence of the posterior covariance of the Kalman filters. One edge in the nominal graph is selected for the visualization. $\lambda_{ij} = 1$ and $\lambda_{ij} = 0.2$ (middle and right) are set for all $(i,j) \in \mathcal{E}$ whereas $\lambda_{ij} = 0$ (left) is only set for the selected edge and the others remain present.

consensus filter. In addition, accurate tracking is achieved with reduced noise.

Recall that the local convergence indicator (18) is proposed to penalize the RAL estimates, and its boundedness and resemblance of the global tracking error (4) are claimed in Section V, which is visualized in Fig. 9. As can be seen, the CI converges in a similar way to the tracking error, which indicates the formation convergence. The boundedness can be seen from the plot on the right, where the bias term in Theorem 1 is subtracted from the CI.

We have mathematically shown the convergence and optimality of GA-RKF in previous sections, and its numerical validation is provided in Fig. 10, where we compare the trace of the posterior covariance, i.e., $tr(\mathbf{\Lambda}_{ij,k})$ in Algorithm 1 between GA-RKF and its root version RKF using different settings of λ_{ij}. Lemma 2 claims that RKF converges even for a small number of edge observations, but $\lambda_{ij} > 0$ is still necessary to have a bounded covariance. In Fig. 10, RKF diverges when $\lambda_{ij} = 0$ and converges when $\lambda_{ij} = 0.2$. On the other hand, GA-RKF converges even when $\lambda_{ij} = 0$ due to the geometric estimates as observations. Moreover, Proposition 2 shows that GA-RKF is more optimal than RKF when $\lambda_{ij} < 1$ and they are equivalent when $\lambda_{ij} = 1$, which is also corroborated in Fig. 10.

C. PRACTICAL AFC SCENARIOS

Having validated the proposed theories, we now test the GA-RKF in some practical scenarios. Note that we now put the estimators in the control loop, i.e., $\hat{\mathbf{z}}_{ij,k}$ in Algorithm 1 is used for the local controllers in Table 1. We use the tracking
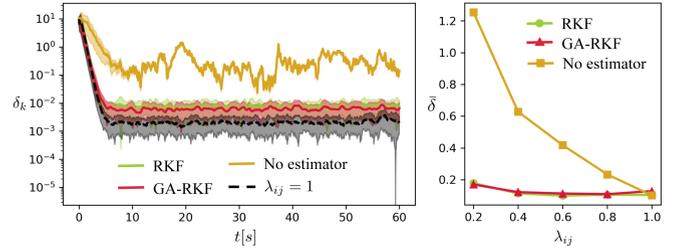
error (4) as our main evaluation metric, and the performance of convergence and optimality of AFC are focused on.

We first set up random edge losses, which cover scenarios S1 and potentially S2 motivated in Section III-A. We simulate the tracking error across a spectrum of λ_{ij}s. Fig. 11 shows the tracking error for the proposed algorithm, where both RKF and GA-RKF have a significant improvement on the average tracking error compared with the case where no estimators are implemented, especially under low λ_{ij}. In the particular case where $\lambda_{ij} = 0.4$ shown on the right in Fig. 11, we see that the convergence speed is maintained compared with the $\lambda_{ij} = 1$ case, where all edge observations are available, which is used as a experimental bound on the tracking error.

Fig. 12 shows another scenario where some agents (followers) are disconnected, which is motivated by S3 in Section III-A, and we expect the rest to remain stable and maintain their respective target positions. As can be seen, the "No estimator" case and RKF diverge with node failure since the underlying topology change requires a new stabilizing controller, if it exists at all, due to graph rigidity requirements. For the RKF, the predictions are outdated as soon as the relative dynamics change without any correction of observations. On the other hand, since the geometry estimates are still accurate as the node failures do not instantly corrupt the geometric pattern. The remaining nodes estimate the edge as if the failed nodes are keeping the formation, and thus could maintain their target positions.

However, a slowed convergence using the GA-RKF can be observed from Fig. 12 if we initiate the node failure at an earlier stage of the formation control. This scenario is different from the random edge loss case, in which the tracking error for the GA-RKF converges at almost the same rate as the no-loss case, even if the losses start at $t = 0$. This is primarily because the weight of the geometric estimation is scaled down by the convergence indicator, such that the inaccurate estimates do not make a strong impact. In the event of node failures, these estimates are the only source of observations, which provide sufficient information for the formation to converge despite not being completely accurate. In conclusion, the GA-RKF is affected if the assumption of sufficient formation convergence is not met, but still yields convergence in the given scenarios. In practice, node failures in the early stages of operation, e.g., battery recharge or repairs, can be rare, but can still be addressed in general with our proposed approach.
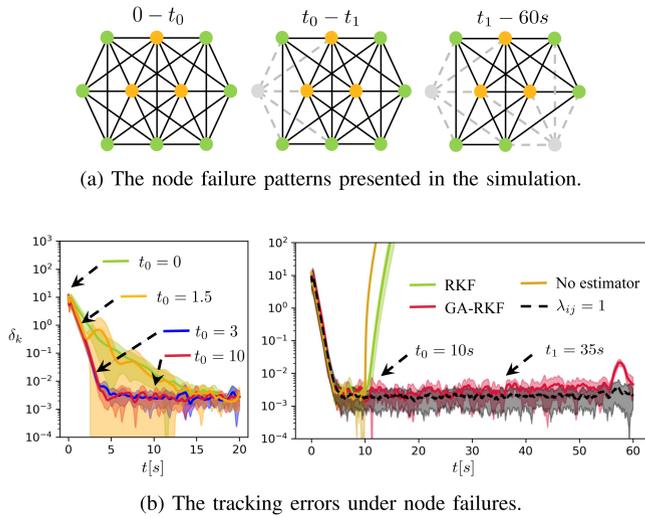
(a) The node failure patterns presented in the simulation.

(b) The tracking errors under node failures.

FIGURE 12. The convergence of the tracking error (left) using GA-RKF when a node detaches from the formation at $t_0 = 0s$, $t_0 = 1.5s$, $t_0 = 3s$, and $t_0 = 10s$. $t_0 = 0$ implies a node fails when the formation is at random initialization and has not yet converged. $t = 10$ implies that a node fails when the formation has converged with a small error. The methods are compared using the full pattern (right).

(a)   (b)

FIGURE 13. Simulations with a large network of 50 node in random configuration. The average degree is 7.5 for the sparse graph and 47.8 (almost fully-connected) for the dense graph. (a) Illustration of the same configuration with sparse and dense connections used in the simulation. (b) The percentage of runs that remain stable after randomly disconnecting a different number of nodes over 100 Monte Carlo runs.

Finally, we perform another experiment to study the performance of GA-RKF in larger networks with varying network density. Fig. 13(a) shows a large network of 50 nodes in random configuration, with two interaction graphs, i.e., a sparse and a dense graph. Both these graphs are designed using the same configuration using the algorithm in [26], and both graphs yield formation convergence. Once convergence is established for the formation, a random subset of nodes is disconnected from the formation to study the performance of GA-RKF given these graphs. We consider different percentages of random node failures in the network, i.e., $0\%, 6\%, 10\%, 30\%, 50\%$. For each of these cases, we implement the GA-RKF algorithm over 100 Monte Carlo runs, and the runs that remain converged after disconnecting the agents are counted and plotted in Fig. 13(b). The results show that the success rates for both sparse and dense networks decrease with increasing number of failed nodes. More specifically, in the case of a dense graph 76% of the runs remain stable with only 25 nodes (50%) missing, while for a sparse graph, only 6% of the runs remain stable for the same percentage of node loss. This represents a much larger capacity and robustness against failed nodes in a dense network than in a sparse network, with the potential trade-off being higher communication and computation load.

VII. CONCLUSION
In this work, we propose the GA-RKF algorithm to enhance the robustness of AFC to topological changes induced by observation losses. Our algorithm adaptively fuses temporal and spatial (geometrical) information using a Kalman filtering framework, resulting in convergence in extreme settings as
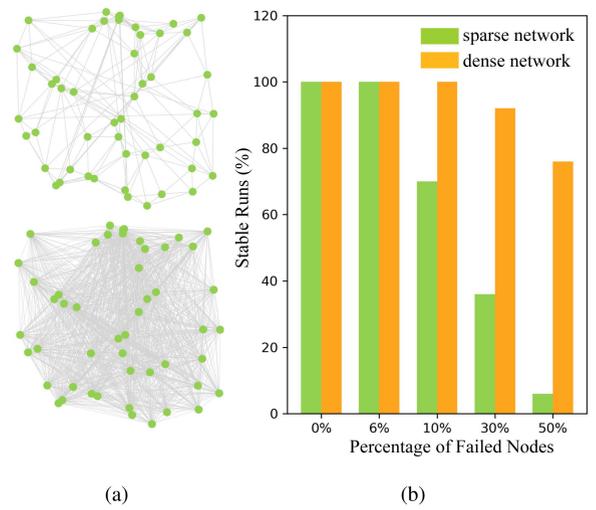
demonstrated by both theoretical results and numerical experiments. We have also shown the practical applicability of GA-RKF in random edge loss and permanent node failure scenarios. As an engineering insight, the system is more robust if the network is designed to have more connections among the agents, allowed by the computation and communication constraints. In our future work, we aim to strengthen several aspects of our proposed framework further. First, the discussions are limited to the edge availability and node departures w.r.t. followers. Furthermore, we would like to generalize our solutions to general directed graphs.

APPENDIX A DERIVATION OF THE COVARIANCES (15) AND (17)
Given model (12) and estimator (14), we have

$$\hat{z}_{ij,k}^{\text{ral}} = \boldsymbol{Y}_{i,k}\boldsymbol{H}_{i,k}^{\dagger}\boldsymbol{p}_{ij} = \left(\boldsymbol{\Theta}_k^*\boldsymbol{H}_{i,k} + \boldsymbol{V}_{i,k}\right)\boldsymbol{H}_{i,k}^{\dagger}\boldsymbol{p}_{ij}, \quad (24)$$

where $\boldsymbol{V}_{i,k}$ is the stochastic element. Applying the property of vectorization and the Kronecker product (see (520) in [37]), the covariance of the estimator is

$$\text{cov}(\hat{z}_{ij,k}^{\text{ral}}) = \text{cov}\left(\text{vec}\left(\hat{z}_{ij,k}^{\text{ral}}\right)\right) \quad (25a)$$

$$= \text{cov}(\text{vec}(\boldsymbol{V}_{i,k}\boldsymbol{H}_{i,k}^{\dagger}\boldsymbol{p}_{ij})) \quad (25b)$$

$$= \text{cov}\left(\left(\boldsymbol{p}_{ij}^{\top}\boldsymbol{H}_{i,k}^{\dagger\top} \otimes \boldsymbol{I}_D\right)\text{vec}(\boldsymbol{V}_{i,k})\right) \quad (25c)$$

$$= \left(\boldsymbol{p}_{ij}^{\top}\boldsymbol{H}_{i,k}^{\dagger\top} \otimes \boldsymbol{I}_D\right)\left(\boldsymbol{I}_{N_{i,k}} \otimes \boldsymbol{R}_{ij}\right)$$
$$\left(\boldsymbol{p}_{ij}^{\top}\boldsymbol{H}_{i,k}^{\dagger\top} \otimes \boldsymbol{I}_D\right)^{\top}, \quad (25d)$$

where we assume the noise vector $\boldsymbol{v}_{ij}$ across the edges are i.i.d. with covariance $\boldsymbol{R}_{ij}$.

TABLE 2. Solutions for (13) with additional constraints.

	General	Translation	Scaling	Rotation	Similarity
constraints	-	$\Theta_k^* = I_D$	Θ_k^* is diagonal	$\Theta_k^{*\top}\Theta_k^* = I_D$	$\Theta_k^{*\top}\Theta_k^* = s_k^2 I_D$
solutions	(13)	$\hat{\Theta}_{i,k}^{\text{ral}} = I_D$	$\hat{\Theta}_{i,k}^{\text{ral}} = \text{diag}(\hat{s}_{1,k}, ..., \hat{s}_{D,k})$	$Y_{i,k}H_{i,k}^\top = U_{i,k}\Sigma_{i,k}\Phi_{i,k}^\top$ $\hat{\Theta}_{i,k}^{\text{ral}} = U_{i,k}\Phi_{i,k}^\top$	$\hat{s}_{i,k} = \frac{1}{D}\text{tr}\left(\Sigma_{i,k}^{H}{}^{-1}\Sigma_{i,k}^{Y}\right)$ $\hat{\Theta}_{i,k}^{\text{ral}} = \hat{s}_{i,k}U_{i,k}\Phi_{i,k}^\top$
minimum $N_{i,k}$	D	0	1	$D-1$	$D-1$

For the covariance of $\hat{z}_{ij,k}^{\text{geo}} = \hat{\Theta}_{i,k}p_{ij}$, we first apply the result in [31] that $\text{cov}(\hat{\theta}_{i,k}) = \frac{1}{N^2}\sum_{i=1}^N \text{cov}(\hat{\theta}_{i,k}^{\text{ral}})$, where $\hat{\theta}_{i,k} = \text{vec}\left(\hat{\Theta}_{i,k}\right)$ and $\hat{\theta}_{i,k}^{\text{ral}} = \text{vec}\left(\hat{\Theta}_{i,k}^{\text{ral}}\right)$. We could then establish that

$$\text{vec}\left(\hat{z}_{ij,k}^{\text{geo}}\right) = \text{vec}(\hat{\Theta}_{i,k}p_{ij}) = \left(p_{ij}^\top \otimes I_D\right)\hat{\theta}_{i,k}, \quad (26)$$

which leads to

$$\text{cov}\left(\text{vec}\left(\hat{z}_{ij,k}^{\text{geo}}\right)\right) = \left(p_{ij}^\top \otimes I_D\right)\text{cov}\left(\hat{\theta}_{i,k}\right)\left(p_{ij}^\top \otimes I_D\right)^\top \quad (27a)$$

$$= \left(p_{ij}^\top \otimes I_D\right)\frac{1}{N^2}\sum_{i=1}^N \text{cov}\left(\hat{\theta}_{i,k}^{\text{ral}}\right)\left(p_{ij}^\top \otimes I_D\right)^\top, \quad (27b)$$

where $\text{cov}(\hat{\theta}_{i,k}^{\text{ral}})$ can be derived similar to (25) as

$$\text{cov}\left(\hat{\theta}_{i,k}^{\text{ral}}\right) = \text{cov}\left(\text{vec}\left(\hat{\Theta}_{i,k}^{\text{ral}}\right)\right) \quad (28a)$$

$$= \text{cov}\left(\left(H_{i,k}^{\dagger\top} \otimes I_D\right)\text{vec}\left(V_{i,k}\right)\right) \quad (28b)$$

$$= \left(H_{i,k}^{\dagger\top} \otimes I_D\right)\left(I_{N_{i,k}} \otimes R_{ij}\right)\left(H_{i,k}^{\dagger\top} \otimes I_D\right)^\top. \quad (28c)$$

With a straightforward substitution, we could obtain

$$\text{cov}\left(\hat{z}_{ij,k}^{\text{geo}}\right) = \left(p_{ij}^\top H_{i,k}^{\dagger\top} \otimes I_D\right)\frac{1}{N^2}\sum_{i=1}^N\left(I_{N_{i,k}} \otimes R_{ij}\right)$$

$$\left(p_{ij}^\top H_{i,k}^{\dagger\top} \otimes I_D\right)^\top, \quad (29)$$

which, if considering identical local covariance for RAL estimates across the nodes, supports the simple approximation in (17), i.e., $\text{cov}(\hat{z}_{ij,k}^{\text{geo}}) = \text{cov}\left(\hat{z}_{ij,k}^{\text{ral}}\right)/N$.

APPENDIX B CONSTRAINED RAL

In this section, we give an overview of the solutions when the formation is restricted to special cases of affine transformations. An overview of these constrained problems and their solutions is shown in Table 2.

Translation only: Translation is dictated by the t_k^* vector in (2), and the shape of the geometry is not changed. As such, the estimation of Θ_k^* can simply be set to $\hat{\Theta}_{i,k} = I_D$.

Scaling only: For cases where only scaling is involved, the parameter matrix Θ_k^* degenerates to

$$\Theta_k^* = \text{diag}\left(s_k^1, ..., s_k^D\right), \quad (30)$$

where $s_k^d \in \mathbb{R}$, for $d = 1, \ldots, D$, scales each dimension. Since the diagonality of Θ_k^* decouples the dimensions in (13), the problem could be decomposed into D simple independent least-squares problems.

Rotation only: The parameter matrix Θ_k^* in this case is an orthogonal rotation matrix with orthonormal columns, i.e., $\Theta_k^{*\top}\Theta_k^* = I_D$ is constrained for (13). This formulation is recognized as the orthogonal Procrustes problem with analytical solutions available [38]. As presented in Table 2, the solution is derived from a singular value decomposition (SVD) $Y_{i,k}H_{i,k}^\top = U_{i,k}\Sigma_{i,k}\Phi_{i,k}^\top$ where $U_{i,k}$ and $\Phi_{i,k}$ contain the singular vectors and $\Sigma_{i,k}$ with singular values.

Similarity transform: Similarity transform is a combination of rotation and scaling, where each dimension is uniformly scaled by a non-negative s_k. Hence, the constraints on Θ_k^* can be relaxed with a scaling ambiguity, as shown in Table 2. The rotation and scaling can be estimated independently, with the rotation estimated as in the previous rotation-only case. For the scaling, if $H_{i,k}$ and $Y_{i,k}$ both have economy-sized SVD with $\Sigma_{i,k}^H$ and $\Sigma_{i,k}^Y$ as the respective diagonal matrices with singular values, s_k can be estimated by $\hat{s}_{i,k} = \frac{1}{D}tr(\Sigma_{i,k}^{H}{}^{-1}\Sigma_{i,k}^{Y})$.

APPENDIX C CONVERGENCE INDICATOR (CI)
A. PROOF OF LEMMA 1

Proof: In the noiseless case, model (12) becomes $Y_{i,k} = Z_k B_{i,k} = \Theta_k^* H_{i,k}$, and the solution to (13) becomes $\hat{\Theta}_{i,k}^{\text{ral}} = Z_k B_{i,k} H_{i,k}^\dagger$, where $B_{i,k}$ is the incidence block for agent i in the time-varying functional graph. Multiplying $B_{i,k}$ on both sides of definition (2) gives $Z_k^* B_{i,k} = \Theta_k^* P B_{i,k} = \Theta_k^* H_{i,k}$, which yields $\Theta_k^* = Z_k^* B_{i,k} H_{i,k}^\dagger$. Then (18) can be rewritten as follows

$$\psi_{i,k} = \frac{1}{N_{i,k}}\sum_{j\in\mathcal{N}_{i,k}}\left\|\left(\hat{\Theta}_{i,k}^{\text{ral}} - \Theta_k^*\right) - \left(\hat{\Theta}_{j,k}^{\text{ral}} - \Theta_k^*\right)\right\|_F^2 \quad (31a)$$

$$= \frac{1}{N_{i,k}}\sum_{j\in\mathcal{N}_{i,k}}\left\|(Z_k - Z_k^*)\left(B_{i,k}H_{i,k}^\dagger - B_{j,k}H_{j,k}^\dagger\right)\right\|_F^2 \quad (31b)$$

$$\leq \frac{1}{N_{i,k}} \sum_{j \in \mathcal{N}_{i,k}} \left\| \boldsymbol{B}_{i,k} \boldsymbol{H}_{i,k}^{\dagger} - \boldsymbol{B}_{j,k} \boldsymbol{H}_{j,k}^{\dagger} \right\|_{\mathrm{F}}^{2} \| \boldsymbol{Z}_k - \boldsymbol{Z}_k^* \|_{\mathrm{F}}^{2} \tag{31c}$$

$$\leq \frac{N}{N_{i,k}} \sum_{j \in \mathcal{N}_{i,k}} \left\| \boldsymbol{B}_{i,k} \boldsymbol{H}_{i,k}^{\dagger} - \boldsymbol{B}_{j,k} \boldsymbol{H}_{j,k}^{\dagger} \right\|_{\mathrm{F}}^{2} \delta_k \tag{31d}$$

$$\leq c_{i,k} \delta_k, \tag{31e}$$

and hence proven. ∎

B. PROOF OF THEOREM 1

Recollect the definition of CI (18), we have

$$\psi_{i,k} = \frac{1}{N_{i,k}} \sum_{j \in \mathcal{N}_{i,k}} \left\| \left(\hat{\boldsymbol{\Theta}}_{i,k}^{\mathrm{ral}} - \boldsymbol{\Theta}_k^* \right) - \left(\hat{\boldsymbol{\Theta}}_{j,k}^{\mathrm{ral}} - \boldsymbol{\Theta}_k^* \right) \right\|_{\mathrm{F}}^{2} \tag{32a}$$

$$= \frac{1}{N_{i,k}} \sum_{j \in \mathcal{N}_{i,k}} \| (\boldsymbol{Z}_k - \boldsymbol{Z}_k^*) \left(\boldsymbol{B}_{i,k} \boldsymbol{H}_{i,k}^{\dagger} - \boldsymbol{B}_{j,k} \boldsymbol{H}_{j,k}^{\dagger} \right)$$
$$+ \left(\boldsymbol{V}_{i,k} \boldsymbol{H}_{i,k}^{\dagger} - \boldsymbol{V}_{j,k} \boldsymbol{H}_{j,k}^{\dagger} \right) \|_{\mathrm{F}}^{2} \tag{32b}$$

$$= \psi_{i,k}' + \psi_{i,k}'' + \psi_{i,k}''', \tag{32c}$$

where the expressions for $\psi_{i,k}'$, $\psi_{i,k}''$ and $\psi_{i,k}'''$ are given by

$$\psi_{i,k}' = \frac{1}{N_{i,k}} \sum_{j \in \mathcal{N}_{i,k}} \left\| (\boldsymbol{Z}_k - \boldsymbol{Z}_k^*) \left(\boldsymbol{B}_{i,k} \boldsymbol{H}_{i,k}^{\dagger} - \boldsymbol{B}_{j,k} \boldsymbol{H}_{j,k}^{\dagger} \right) \right\|_{\mathrm{F}}^{2} \tag{33a}$$

$$\psi_{i,k}'' = \frac{1}{N_{i,k}} \sum_{j \in \mathcal{N}_{i,k}} \left\| \boldsymbol{V}_{i,k} \boldsymbol{H}_{i,k}^{\dagger} - \boldsymbol{V}_{j,k} \boldsymbol{H}_{j,k}^{\dagger} \right\|_{\mathrm{F}}^{2} \tag{33b}$$

$$\psi_{i,k}''' = \frac{2}{N_{i,k}} \sum_{j \in \mathcal{N}_{i,k}} tr \left(\left(\boldsymbol{B}_{i,k} \boldsymbol{H}_{i,k}^{\dagger} - \boldsymbol{B}_{j,k} \boldsymbol{H}_{j,k}^{\dagger} \right)^{\top} \right.$$
$$\left. (\boldsymbol{Z}_k - \boldsymbol{Z}_k^*)^{\top} \left(\boldsymbol{V}_{i,k} \boldsymbol{H}_{i,k}^{\dagger} - \boldsymbol{V}_{j,k} \boldsymbol{H}_{j,k}^{\dagger} \right) \right). \tag{33c}$$

We first define the expectation of the tracking error δ_k and the expectation of CI as

$$\mathbb{E}[\delta_k] = \frac{1}{N} \mathbb{E} \left[\| \boldsymbol{Z}_k - \boldsymbol{Z}_k^* \|_{\mathrm{F}}^{2} \right], \tag{34}$$

$$\mathbb{E}[\psi_{i,k}] = \mathbb{E} \left[\psi_{i,k}' \right] + \mathbb{E} \left[\psi_{i,k}'' \right] + \mathbb{E} \left[\psi_{i,k}''' \right], \tag{35}$$

respectively, and we then analyze each term individually.

Since $\psi_{i,k}'$ is the same as (31b), we have

$$\mathbb{E}[\psi_{i,k}'] \leq \mathbb{E} \left[\frac{1}{N_{i,k}} \sum_{j \in \mathcal{N}_{i,k}} \left\| \boldsymbol{B}_{i,k} \boldsymbol{H}_{i,k}^{\dagger} - \boldsymbol{B}_{j,k} \boldsymbol{H}_{j,k}^{\dagger} \right\|_{\mathrm{F}}^{2} \right.$$
$$\left. \| \boldsymbol{Z}_k - \boldsymbol{Z}_k^* \|_{\mathrm{F}}^{2} \right] \tag{36a}$$

$$= \frac{N}{N_{i,k}} \sum_{j \in \mathcal{N}_{i,k}} \left\| \boldsymbol{B}_{i,k} \boldsymbol{H}_{i,k}^{\dagger} - \boldsymbol{B}_{j,k} \boldsymbol{H}_{j,k}^{\dagger} \right\|_{\mathrm{F}}^{2} \mathbb{E}[\delta_k]. \tag{36b}$$

For term $\mathbb{E}[\psi_{i,k}'']$ in (35),

$$\mathbb{E}[\psi_{i,k}''] = \frac{1}{N_{i,k}} \sum_{j \in \mathcal{N}_{i,k}} tr \left(\boldsymbol{H}_{i,k}^{\dagger\top} \mathbb{E}[\boldsymbol{V}_{i,k}^{\top} \boldsymbol{V}_{i,k}] \boldsymbol{H}_{i,k}^{\dagger} \right)$$
$$+ tr \left(\boldsymbol{H}_{j,k}^{\dagger\top} \mathbb{E}[\boldsymbol{V}_{j,k}^{\top} \boldsymbol{V}_{j,k}] \boldsymbol{H}_{j,k}^{\dagger} \right)$$
$$- 2 tr \left(\boldsymbol{H}_{i,k}^{\dagger\top} \mathbb{E}[\boldsymbol{V}_{i,k}^{\top} \boldsymbol{V}_{j,k}] \boldsymbol{H}_{j,k}^{\dagger} \right) \tag{37a}$$

$$= \frac{1}{N_{i,k}} \sum_{j \in \mathcal{N}_{i,k}} tr \left(\boldsymbol{R}_{ij} \right) tr \left(\boldsymbol{H}_{i,k}^{\dagger\top} \boldsymbol{H}_{i,k}^{\dagger} \right)$$
$$+ tr(\boldsymbol{R}_{ij}) tr \left(\boldsymbol{H}_{j,k}^{\dagger\top} \boldsymbol{H}_{j,k}^{\dagger} \right) + 0 \tag{37b}$$

$$= \frac{tr(\boldsymbol{R}_{ij})}{N_{i,k}} \sum_{j \in \mathcal{N}_{i,k}} \left\| \boldsymbol{H}_{i,k}^{\dagger} \right\|_{\mathrm{F}}^{2} + \left\| \boldsymbol{H}_{j,k}^{\dagger} \right\|_{\mathrm{F}}^{2}, \tag{37c}$$

where we use Property 1 in Appendix C. Finally, for term $\mathbb{E}[\psi_{i,k}''']$ in (35), we have

$$\mathbb{E}[\psi_{i,k}'''] = \mathbb{E} \left[\frac{1}{N_{i,k}} \sum_{j \in \mathcal{N}_{i,k}} tr \left(\left(\boldsymbol{B}_{i,k} \boldsymbol{H}_{i,k}^{\dagger} - \boldsymbol{B}_{j,k} \boldsymbol{H}_{j,k}^{\dagger} \right)^{\top} \right. \right.$$
$$\left. \left. (\boldsymbol{Z}_k - \boldsymbol{Z}_k^*)^{\top} \left(\boldsymbol{V}_{i,k} \boldsymbol{H}_{i,k}^{\dagger} - \boldsymbol{V}_{j,k} \boldsymbol{H}_{j,k}^{\dagger} \right) \right) \right] \tag{38a}$$

$$= \frac{1}{N_{i,k}} \sum_{j \in \mathcal{N}_{i,k}} tr \left(\left(\boldsymbol{B}_{i,k} \boldsymbol{H}_{i,k}^{\dagger} - \boldsymbol{B}_{j,k} \boldsymbol{H}_{j,k}^{\dagger} \right)^{\top} \right.$$
$$\left. \mathbb{E}[\boldsymbol{Z}_k - \boldsymbol{Z}_k^*]^{\top} \left(\mathbb{E}[\boldsymbol{V}_{i,k}] \boldsymbol{H}_{i,k}^{\dagger} - \mathbb{E}[\boldsymbol{V}_{j,k}] \boldsymbol{H}_{j,k}^{\dagger} \right) \right)$$
$$= 0, \tag{38b}$$

as the noises in matrices $\boldsymbol{V}_{i,k}$ for all i and k are zero-mean and uncorrelated with $\boldsymbol{Z}_k - \boldsymbol{Z}_k^*$. Combing the expressions (36), (37) and (38), we can conclude that

$$\mathbb{E}[\psi_{i,k}] \leq c_{i,k} \mathbb{E}[\delta_k] + b_{i,k}, \tag{39}$$

where $c_{i,k}$ and $b_{i,k}$ are given by (20) in Theorem 1.

C. EXPECTATION OF NOISE MATRIX INNER PRODUCTS

Property 1: Given a matrix $\boldsymbol{V} = [\boldsymbol{v}_1, \boldsymbol{v}_2, \ldots, \boldsymbol{v}_N] \in \mathbb{R}^{D \times N}$ where $\boldsymbol{v}_i \stackrel{\text{i.i.d}}{\sim} \mathcal{N}(\boldsymbol{0}_D, \boldsymbol{R})$ for $i = 1, \ldots, N$, the following statement holds true

$$\mathbb{E}[\boldsymbol{V}^{\top} \boldsymbol{V}] = tr(\boldsymbol{R}) \boldsymbol{I}_N. \tag{40}$$

Proof: If we use i and j to denote the matrix row and column index, respectively, then elements in matrix $\mathbb{E}[\boldsymbol{V}^T \boldsymbol{V}]$ are

$$[\mathbb{E}[\boldsymbol{V}^{\top} \boldsymbol{V}]]_{ij} = \begin{cases} \mathbb{E}[\boldsymbol{v}_i^{\top} \boldsymbol{v}_j], & i = j \\ 0, & \text{otherwise} \end{cases}, \tag{41}$$

since $\boldsymbol{v}_i$ and $\boldsymbol{v}_j$ are independent for any $i = 1, 2, \ldots, N$ and $j \neq i$. In addition, the expectation of $\boldsymbol{v}_i^{\top} \boldsymbol{v}_i$ is the sum of the variance of each element in the vector i.e., $\mathbb{E}[\boldsymbol{v}_i^{\top} \boldsymbol{v}_i] = \mathrm{tr}[\boldsymbol{R}]$.

Moreover, since the vectors are also identically distributed, we have $\mathbb{E}[V^\top V] = \text{tr}[R]I_N$, and hence proven. ∎

REFERENCES

[1] Z. Li and R. T. Rajan, "Geometry-aware distributed Kalman filtering for affine formation control under observation losses," in *Proc. 26th Int. Conf. Inf. Fusion*, 2023, pp. 1–7.

[2] A. Heuillet, F. Couthouis, and N. Díaz-Rodríguez, "Collective explainable AI: Explaining cooperative strategies and agent contribution in multiagent reinforcement learning with Shapley values," *IEEE Comput. Intell. Mag.*, vol. 17, no. 1, pp. 59–71, Feb. 2022.

[3] Y. Rizk, M. Awad, and E. W. Tunstel, "Cooperative heterogeneous multi-robot systems: A survey," *ACM Comput. Surv.*, vol. 52, no. 2, pp. 1–31, 2019.

[4] R. Ureña, G. Kou, Y. Dong, F. Chiclana, and E. Herrera-Viedma, "A review on trust propagation and opinion dynamics in social networks and group decision making frameworks," *Inf. Sci.*, vol. 478, pp. 461–475, 2019.

[5] G. Zhao, H. Cui, and C. Hua, "Hybrid event-triggered bipartite consensus control of multiagent systems and application to satellite formation," *IEEE Trans. Autom. Sci. Eng.*, vol. 20, no. 3, pp. 1760–1771, Jul. 2023.

[6] R. T. Rajan et al., "Applications and potentials of intelligent swarms for magnetospheric studies," *Acta Astronautica*, vol. 193, pp. 554–571, 2022.

[7] J. Alonso-Mora, S. Baker, and D. Rus, "Multi-robot formation control and object transport in dynamic environments via constrained optimization," *Int. J. Robot. Res.*, vol. 36, no. 9, pp. 1000–1021, 2017.

[8] G.-P. Liu and S. Zhang, "A survey on formation control of small satellites," *Proc. IEEE*, vol. 106, no. 3, pp. 440–457, Mar. 2018.

[9] K. A. Ghamry and Y. Zhang, "Cooperative control of multiple UAVs for forest fire monitoring and detection," in *Proc. 12th IEEE/ASME Int. Conf. Mechatronic Embedded Syst. Appl.*, 2016, pp. 1–6.

[10] S.-M. Kang, M.-C. Park, B.-H. Lee, and H.-S. Ahn, "Distance-based formation control with a single moving leader," in *Proc. Amer. Control Conf.*, 2014, pp. 305–310.

[11] D. V. Vu, M. H. Trinh, P. D. Nguyen, and H.-S. Ahn, "Distance-based formation control with bounded disturbances," *IEEE Control Syst. Lett.*, vol. 5, no. 2, pp. 451–456, Apr. 2021.

[12] S. Zhao and D. Zelazo, "Translational and scaling formation maneuver control via a bearing-based approach," *IEEE Trans. Control Netw. Syst.*, vol. 4, no. 3, pp. 429–438, Sep. 2017.

[13] J. Zhao, X. Li, X. Yu, and H. Wang, "Finite-time cooperative control for bearing-defined leader-following formation of multiple double-integrators," *IEEE Trans. Cybern.*, vol. 52, no. 12, pp. 13363–13372, Dec. 2022.

[14] Z. Lin, L. Wang, Z. Chen, M. Fu, and Z. Han, "Necessary and sufficient graphical conditions for affine formation control," *IEEE Trans. Autom. Control*, vol. 61, no. 10, pp. 2877–2891, Oct. 2016.

[15] S. Zhao, "Affine formation maneuver control of multiagent systems," *IEEE Trans. Autom. Control*, vol. 63, no. 12, pp. 4140–4155, Dec. 2018.

[16] X.-M. Zhang et al., "Networked control systems: A survey of trends and techniques," *IEEE/CAA J. Automatica Sinica*, vol. 7, no. 1, pp. 1–17, Jan. 2020.

[17] X. Dong and G. Hu, "Time-varying formation control for general linear multi-agent systems with switching directed topologies," *Automatica*, vol. 73, pp. 47–55, 2016.

[18] Z. Wang, T. Liu, and Z.-P. Jiang, "Cooperative formation control under switching topology: An experimental case study in multirotors," *IEEE Trans. Cybern.*, vol. 51, no. 12, pp. 6141–6153, Dec. 2021.

[19] Y. Zhai, Z.-W. Liu, Z.-H. Guan, and G. Wen, "Resilient consensus of multi-agent systems with switching topologies: A trusted-region-based sliding-window weighted approach," *IEEE Trans. Circuits Syst. II, Exp. Briefs*, vol. 68, no. 7, pp. 2448–2452, Jul. 2021.

[20] G. Franzè, A. Casavola, D. Famularo, and W. Lucia, "Distributed receding horizon control of constrained networked leader–follower formations subject to packet dropouts," *IEEE Trans. Control Syst. Technol.*, vol. 26, no. 5, pp. 1798–1809, Sep. 2018.

[21] X. Gong, Y.-J. Pan, J.-N. Li, and H. Su, "Leader following consensus for multi-agent systems with stochastic packet dropout," in *Proc. 10th IEEE Int. Conf. Control Automat.*, 2013, pp. 1160–1165.

[22] J. Lee et al., "Relative navigation with intermittent laser-based measurement for spacecraft formation flying," *J. Astron. Space Sci.*, vol. 35, no. 3, pp. 163–173, 2018.

[23] L. Sedghi, J. John, M. Noor-A-Rahim, and D. Pesch, "Formation control of automated guided vehicles in the presence of packet loss," *Sensors*, vol. 22, no. 9, 2022, Art. no. 3552.

[24] M. V. Der Marel and R. T. Rajan, "Distributed Kalman filters for relative formation control of multi-agent systems," in *Proc. 30th Eur. Signal Process. Conf.*, 2022, pp. 1422–1426.

[25] Y. Xu, D. Luo, Y. You, and H. Duan, "Affine transformation based formation maneuvering for discrete-time directed networked systems," *Sci. China Technological Sci.*, vol. 63, no. 1, pp. 73–85, 2020.

[26] Z. Li, G. Leus, and R. T. Rajan, "Fast multiagent formation stabilization with sparse universally rigid frameworks," in *Proc. 33rd Eur. Signal Process. Conf.*, 2025, pp. 2392–2396.

[27] F. Xiao, Q. Yang, X. Zhao, and H. Fang, "A framework for optimized topology design and leader selection in affine formation control," *IEEE Robot. Automat. Lett.*, vol. 7, no. 4, pp. 8627–8634, Oct. 2022.

[28] Y. Xu, S. Zhao, D. Luo, and Y. You, "Affine formation maneuver control of multi-agent systems with directed interaction graphs," in *Proc. 37th Chin. Control Conf.*, 2018, pp. 4563–4568.

[29] H. Su, Z. Yang, S. Zhu, and C. Chen, "Bearing-based formation maneuver control of leader-follower multi-agent systems," *IEEE Control Syst. Lett.*, vol. 7, pp. 1554–1559, 2023.

[30] Y. Bar-Shalom, P. K. Willett, and X. Tian, *Tracking and Data Fusion*, vol. 11, Storrs, CT, USA: YBS Publishing Storrs, 2011.

[31] R. Olfati-Saber and J. Shamma, "Consensus filters for sensor networks and distributed sensor fusion," in *Proc. 44th IEEE Conf. Decis. Control*, 2005, pp. 6698–6703.

[32] G. Wen, W. Yu, Z. Duan, and P. Wang, "Consensus of multi-agent systems with intermittent communication and its extensions," in *Handbook of Real-Time Computing.*, Berlin, Germany: Springer, 2022, pp. 1143–1197.

[33] B. Sinopoli, L. Schenato, M. Franceschetti, K. Poolla, M. Jordan, and S. S. Sastry, "Kalman filtering with intermittent observations," *IEEE Trans. Autom. Control*, vol. 49, no. 9, pp. 1453–1464, Sep. 2004.

[34] G. N. Nair and R. J. Evans, "Stabilizability of stochastic linear systems with finite feedback data rates," *SIAM J. Control Optim.*, vol. 43, no. 2, pp. 413–436, 2004.

[35] P. Tichavsky, C. H. Muravchik, and A. Nehorai, "Posterior Cramér-Rao bounds for discrete-time nonlinear filtering," *IEEE Trans. Signal Process.*, vol. 46, no. 5, pp. 1386–1396, May 1998.

[36] R. A. Horn and C. R. Johnson, *Matrix Analysis.*, Cambridge, U.K.: Cambridge Univ. Press, 2012.

[37] K. B. Petersen et al., "The matrix cookbook," Technical University of Denmark, vol. 7, no. 15, 2008, Art. no. 510.

[38] P. H. Schönemann, "A generalized solution of the orthogonal procrustes problem," *Psychometrika*, Springer-Verlag, vol. 31, no. 1, pp. 1–10, 1966.

ZHONGGANG LI (Graduate Student Member, IEEE) received the M.Sc. *(cum laude)* degree in electrical engineering from the Delft University of Technology, Delft, The Netherlands, where he is currently working toward the Ph.D. degree with Signal Processing Systems Group, Faculty of Electrical Engineering, Mathematics and Computer Science. He is a Researcher with Delft Sensor AI Lab. His research interests include distributed signal processing and control for multiagent systems.

RAJ THILAK RAJAN (Senior Member, IEEE) received the Ph.D. degree in electrical engineering from the Delft University of Technology, Delft, The Netherlands, in 2016. He is currently an Assistant Professor with the Faculty of Electrical Engineering, Mathematics and Computer Science, Delft University of Technology, Master Coordinator of signals and systems, and Co-Director of the Delft Sensor AI Lab. His research interests include signal processing theory and methods for distributed autonomous sensing systems. He is an Elected Member of the IAF SCAN (Space Communications and Navigation) Committee, IEEE ASI (Autonomous Systems Initiative), and Associate Editor for IEEE OPEN JOURNAL OF SIGNAL PROCESSING.